ELSEVIER

De novo design of allochroic zwitterions

Dong Zhang [1], Yijing Tang [1], Jintao Yang [2,*], Yijing Gao [3], Chunxin Ma [4], Lingbin Che [6], Jianguo Wang [3], Jiang Wu [5], Jie Zheng [1,*]

[1] Department of Chemical, Biomolecular, and Corrosion Engineering, The University of Akron, Ohio 44325, USA
[2] College of Materials Science& Engineering, Zhejiang University of Technology, Hangzhou 310014, China
[3] Institute of Industrial Catalysis, State Key Laboratory Breeding Base of Green-Chemical Synthesis Technology, College of Chemical Engineering, Zhejiang University of Technology, Hangzhou 310032, China
[4] State Key Laboratory of Marine Resources Utilization in South China Sea, Hainan University, Haikou 570228, China
[5] School of Pharmaceutical Sciences, Wenzhou Medical University, Wenzhou 325035, China
[6] Department of Orthopedics, Shanghai General Hospital, Shanghai Jiao Tong University School of Medicine, Shanghai 200080, China

Zwitterionic materials and allochroic materials, as the two completely different materials, offer distinct properties and functions for different applications, where the former is well recognized as bio-inert materials with highly hydrophilic, antifouling, and biocompatible properties, while the latter is proven as stimuli-responsive discoloration materials with poor water solubility and high toxicity to cells. However, the development of zwitterionic, allochroic materials remains great challenging by integrating these oppositely properties into the same materials. Here, we designed and synthesized water-soluble, allochroic, and zwitterionic polymers of (pVPES) with built-in nonfouling and pH-responsive discoloration properties under *in vitro* and *in vivo* conditions. pVPES can serve as a versatile material platform for either self-polymerizing into different architectures (i.e., brushes, colloids, microgels, hydrogels,) or co-polymerization with other functional polymers to become different smart devices (i.e., colorimetric pollutant sensors, electrochromic smart windows, bilayer hydrogel actuators), all realizing the integration of antifouling and allochroic properties. More importantly, pVPES-based hydrogel patches enabled to not only accelerate wound healing of both chronic and acute wounds, but also distinguish chronic wounds from acute wounds in mice by color changes. This work opens new directions for the development of functional zwitterionic materials by integrating allochroic properties into inert materials for bio-optics applications.

Keywords: Zwitterionic materials; Allochroic materials; Biocompatible polymers; Hydrogels

Main

Biocompatible, allochroic polymers have long been attractive materials for bioimaging applications, including disease diagnosis [1], wearable displays [2–4], human–machine interfaces [5], and point-of-care monitoring [6]. There are two main challenges for achieving this goal: excellent nonfouling property and stimuli-responsive color-change property. However, these two distinct properties usually do not co-exist in the same materials, instead compromise each other, simply because the former requires high hydrophilicity to resist unwanted biomolecule adsorption (e.g., protein adsorption, cell adhesion, and fibrous

* Corresponding authors.
E-mail addresses: Yang, J. (yangjt@zjut.edu.cn), Zheng, J. (zhengj@uakron.edu).

 https://doi.org/10.1016/j.mattod.2022.09.001

capsule formation), while the latter often contains polycyclic aromatic hydrocarbons (PAHs) with inter-/intramolecular electron transfer ability to trigger the emission of different visible/invisible colors [7,8]. To date, the vast majority of current studies has been mostly limited to develop antifouling materials and allochroic materials separately, however, biocompatible, allochroic polymers are still very scanty.

Zwitterionic polymers, bearing an equal number of cationic and anionic groups in the same chains while still maintaining an overall charge neutrality [9–11], have demonstrated their nonfouling property against unwanted biomolecule adsorption and subsequent foreign body reaction in many *in vivo* applications [12–16]. However, those zwitterionic polymers, including the most widely used poly(carboxybetaine), poly(sulfobetaine), and poly(phosphorylcholine), do not possess any allochroic property [17,18]. A common strategy to mitigate this issue is to introduce allochroic moieties (e.g., perylene [19], tetraphenylethene [20,21], and indole [22,23]) to zwitterionic polymers via chemical conjugation or physical bonding, but which will compromise their excellent nonfouling property due to strong hydrophobic characteristics of allochroic moieties. In parallel, substantial progress has been made to develop many allochroic materials, including anthocyanin derivatives [24], phosphorescence polymers [25,26], and photonic colloids [27]. But, antifouling mechanisms prevent these allochroic materials from serving as biocompatible or nonfouling materials, because they are mostly hydrophobic with poor water solubility and high toxicity to cells. Moreover, allochroic materials require specific inter- or intra-molecular structural changes (e.g., ring open/close, molecular isomerization, condensed nucleus, and molecular self-aggregation) to trigger optical/color changes from a ground state to an excited state [28–30]. This adds additional challenge to conjugate them with zwitterionic polymers without sacrificing either nonfouling or allochroic property. To the best of our knowledge, no pure zwitterionic polymers with built-in allochroic function have been reported to achieve both nonfouling and color-change properties in complex bio-media and devices.

In this work, we designed and synthesized a pure polymeric zwitterion of poly[2-(1-(4-vinylbenzyl)pyridin-1-ium-4-yl)ethane-1-sulfonate] (pVPES) without adding any allochroic additives to achieve intrinsic, built-in nonfouling and allochroic properties under *in vitro* and *in vivo* conditions. From a structural viewpoint, monomeric VPES contains (i) styryl and pyridine moieties enabling a reversible intramolecular transformation between zwitterion and complex states to trigger the reversible pH-responsive color change and (ii) a zwitterionic quaternary ammonium-sulfonate pair endowing superhydrophilicity and excellent fouling resistance *in vivo*. Specifically, monomeric VPES solution exhibited a very fast, reversible switching between the colorless state in acidic solution and green/cyan colors in basic solution, whose allochroic function is mainly stemmed from the three different intramolecular charge distributions between zwitterionic and styryl groups. Further polymerization of VPES into different polymeric architectures (i.e., brushes, nanoparticles, microgels, and hydrogels) can also retain their stable and reversible pH-/salt-triggered color changes in compatible with antifouling, lubrication/friction, and actuation functions. Finally, by taking advantage of the integrated nonfouling and allochroic properties of pVPES, we further transformed pVPES to different devices for practical applications, including pH sensors for sewage, smart electrochromic windows, allochroic actuators, and synchronous wound healing diagnosis in mice, for demonstrating the zwitterion-induced nonfouling and allochroic properties. This work for the first time discovers a pure zwitterionic polymer with compatible nonfouling and allochroic properties, which explore a new optical function of zwitterionic polymers beyond their traditional nonfouling property.

Design and synthesis of an allochroic zwitterion monomer

First, a zwitterion monomer of 2-(1-(4-vinylbenzyl)pyridin-1-ium-4-yl)ethane-1-sulfonate (VPES) was designed and synthesized by coupling 4-vinylbenzyl chloride (VBC) and 4-pyridinylethanesulfonic acid (PDASNa) via a one-step substitution reaction, whose chemical structure was verified by ^{1}H NMR spectrum (Fig. S1). While the resultant VPES contains hydrophobic moieties of styryl and pyridine, zwitterionic groups of pyridine quaternary ammonium and sulfonate enable strong ionic solvation, thus leading to excellent water solubility (>0.25 g/mL, at 25 °C). As a proof-of-concept, it was the first time to observed that zwitterionic VPES monomers exhibited a reversible color change between the uncolored state in acidic solutions (pH = 0–7) and the green-color state in basic solutions (pH = 8–14). Further investigation of the solvatochromic effect of VPES solutions in an entire pH range (pH = 0–14) revealed the same reversible colorless ↔ green transition at a threshold pH value of 8.0 within a few seconds (Fig. 1a & S2). To better understand the pH-induced color change phenomena, density functional theory (DFT) at PBE0/6–31++G(d, p) level was performed to study photophysical and spectra properties of VPES in the aqueous phase. In Fig. 1b, VPES showed the three distinct electron density distributions (i.e., quaternary ammonium salt (QAS), zwitterion, and complex states) at the highest occupied molecular orbitals (HOMOs) and the lowest unoccupied molecular orbitals (LUMOs). While the electron density of HOMOs of all the studied VPES was localized at different sites of styryl and zwitterionic groups, all of three LUMOs were consistently and predominantly centered on the pyridine moiety of VEPS with small variations. On the basis of relative electron density of the three different VPES states between HOMOs and LUMOs, the complex VPES state had the smallest energy gap of 2.0 eV between HOMO and LUMO, as compared to 2.65 eV at the zwitterion state and 6.25 eV at the QAS state. Consistently, the simulated UV–vis spectra of VPES also displayed three different states, among which the complex VPES state had a single peak at ~370 nm with the lowest peak intensity (Fig. S2), in reasonable agreement with the experimental bands at ~380 nm(and ~612 nm). As a result, the complex state had the fast charge transfer from the HOMO of styryl moiety to the LUMO of pyridine moiety, thus leading to the almost spontaneous response in color change.

To evaluate the pH sensitivity and range of VEPS, we selected a set of commercial pH indicators with a certain degree of water solubility (i.e., litmus, methyl orange, phenolphthalein, anthocyanin, ethyl green, and methyl violet) to cover an entire pH

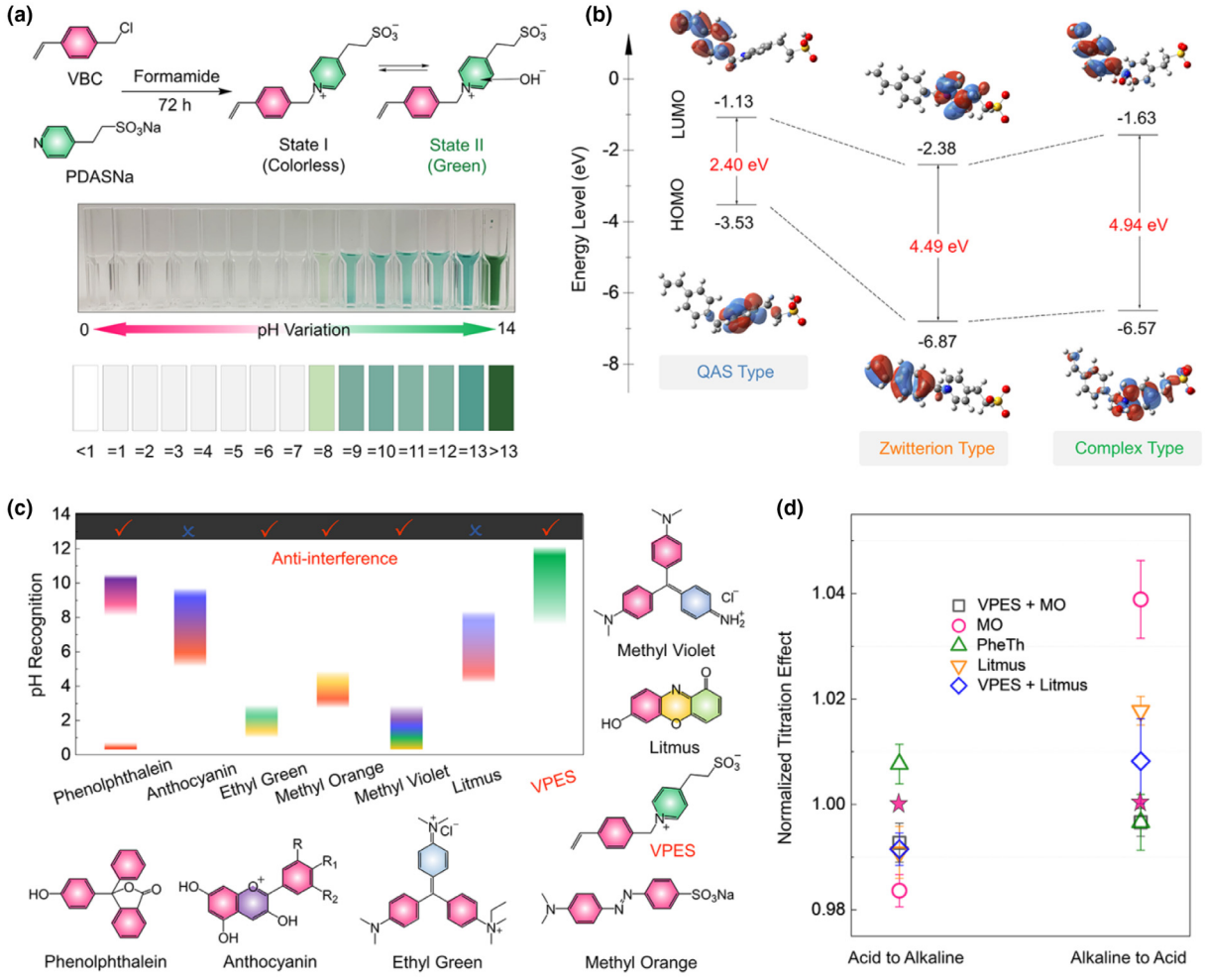

FIGURE 1

Structural and allochroic properties of zwitterionic VPES monomer. (a) Chemical synthesis and structures of zwitterionic VPES, with pH-dependent color change between colorless at pH = 0–7, light green pH = 8–13, and dark green at pH > 13 in water. (b) Three-dimensional contour plots of HOMO and LUMO orbitals of VPES monomers at a QAS state in an acidic medium, a zwitterion state in a neutral medium, and a complex state in an alkaline medium, each with electron density distributions and HOMO–LUMO energy gap (eV) by DFT simulations. (c) Comparison of pH-responsive ranges for inducing color changes for six commercial pH indicators and VPES. (d) pH titration profiles of three single pH indicators (methyl orange (MO), phenolphthalein (PheTh), and litmus) and two binary pH indicators (VPES + methyl orange and VPES + litmus) during both "acid-to-alkaline" and "alkaline-to-acid" processes.

range (0–14) for comparison (Fig. 1c). Among six pH indicators, only litmus and anthocyanin displayed a wider color gamut than VPES, but both suffered from strong interference effect. Different from most of pH indicators that are more sensitive to acidic solutions, VPES covered an alkaline pH range of 7–14 with vibrant color changes between colorless, light green, and dark green, which allows VPES to work with acidic-sensitive pH indicators to cover an entire pH range of 0–14 with distinct color change. To end this, we conducted both "acid-to-alkaline" and "alkaline-to-acid" titration processes to test the pH-dependent color change using five pH indicators alone and in combination, including methyl orange, litmus, phenolphthalein, VPES + methyl orange, and VPES + litmus (Tables S1-2, Fig. S3). pH titrations in Fig. 1d showed that single pH indicators (methyl orange, litmus, and phenolphthalein) were solely limited to either "acid-to-alkaline" or "alkaline-to-acid" titration with large titration deviation (>4%), corresponding to a monoprotonated species. Differently, upon the addition of either acid or alkaline to titration, the binary mixtures of "VPES + methyl orange" and "VPES + litmus" exhibited pH-dependent, multiple color changes of blue-to-purple or pink-to-purple at acidic pH ranges and colorless-to-green at basic pH ranges, leading to small titration deviations of <1%. Such multiple color changes are attributed to a synergistic effect of internal charge transfer between VPES and methyl orange/litmus, resulting from the push–pull effect of the electron-donating tertiary amine /hydroxyphenoxazone moieties and the electron-withdrawing π-conjugated styryl/N=N moieties.

Integrated allochroic and antifouling properties of polyzwitterions with different structural architectures

Different from conventional allochroic molecules that are mostly limited to small organic compounds with poor solubility and high cell toxicity, VPES was purposely designed in a way with highly soluble zwitterionic quaternary ammonium-sulfonate

groups and a double-bond attached to a benzene core, which allows to be polymerized into different polymeric architectures (i.e., polymer brushes, sphere colloids, microgels, and hydrogels, Fig. 2a) for different practical applications. In pVPES, zwitterionic groups enable a typical anti-polyelectrolyte behavior by rendering pVPES to shrink in water, but stretch in salt solution, leading to salt-responsive conformational change for antifouling property, while the co-presence of pyridine group allows for reversible

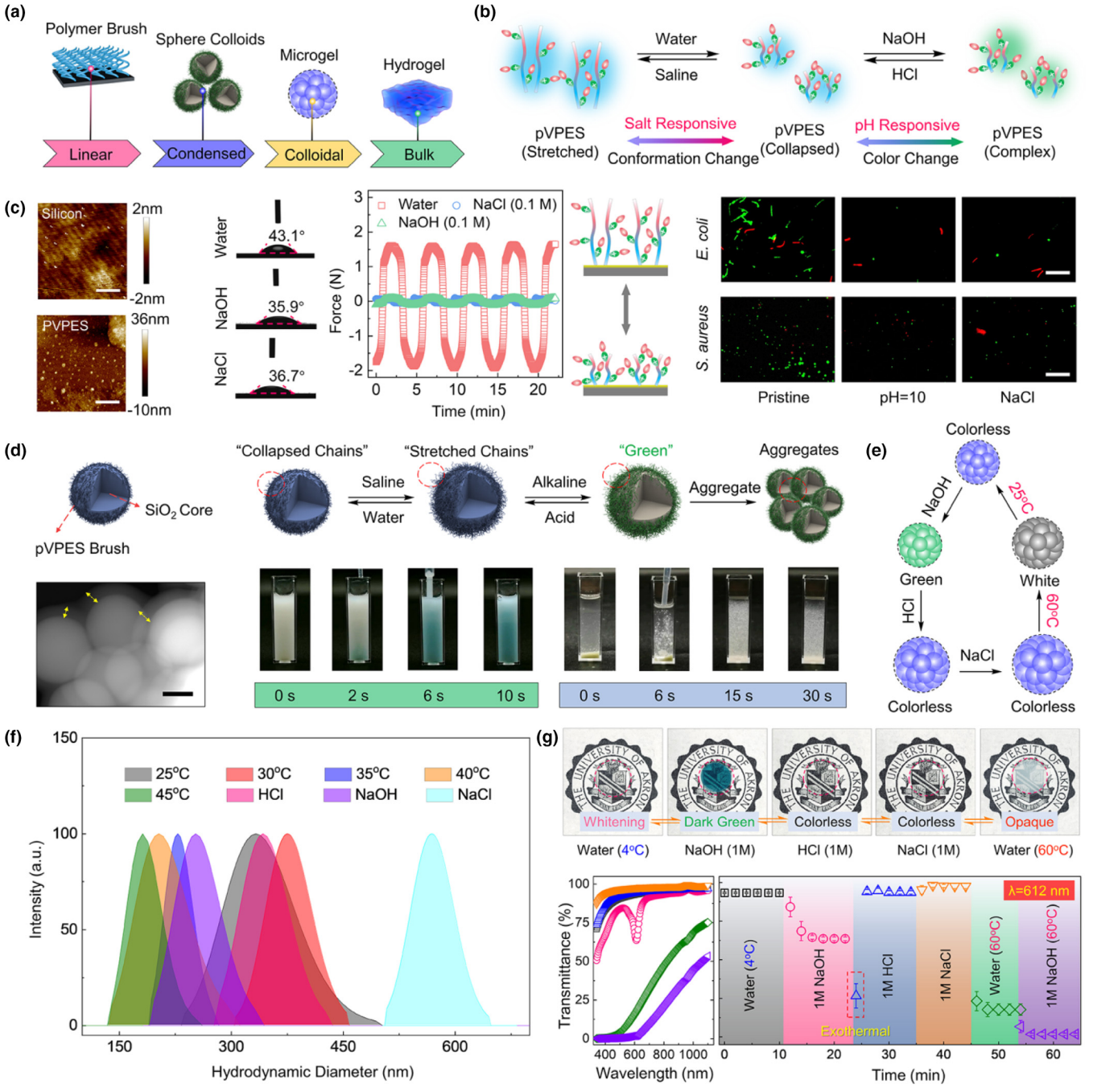

FIGURE 2

Polymorphic, allochroic zwitterions with different functions. (a) Polymorphic pVPES-based zwitterions with different structural architectures including linear polymer brush, condensed sphere NPs, crosslinked microgel, and hydrogel. (b) Zwitterionic-induced color change of pVPES chains in response to salt and pH stimuli. (c) Surface wettability and morphologies of pVPES brushes by AFM images (left), time-dependent surface friction for water-, NaOH-, and saline-treated pVPES brushes (middle), and surface resistance to and contact killing of *E. coli* and *S. aureus* on pVPES brushes before and after treating with alkaline and salt solutions (right). Scale bar: 20 μm. (d) TEM image (scale bar = 100 nm) of pVPES-SiO_2 NPs with a core–shell structure (left) and dual salt- and pH-responsive color changes of pVPES-SiO_2 NPs solutions (right). (e) Schematic of salt- and thermo-responsive color change of PVN microgels and (f) hydrodynamic diameters of PVN microgels under different conditions (Temperature: 25 ~ 45 °C; pH: acid/ alkaline; salt). (g) Visual inspection of color changes of PVN hydrogels on the top of University of Akron logo (top) and optical transmittance of PVN hydrogels treated with different acid, alkaline, salt, and hot (60 °C)/cold (4 °C) water solutions (bottom).

color changes in response to salt and pH stimuli (Fig. 2b). To test this hypothesis, we prepared the four different types of pVPES-based brushes, sphere colloids, chemical-crosslinked microgels, and bulk hydrogels for demonstrating their co-existing antifouling and color-change properties (Fig. 2a & S4). As a first example, linear pVPES brushes were grafted on silicon wafers and Au chips with optimal thickness of ~25–30 nm and roughness of ~1 nm (Fig. 2c). Upon polymerizing and grafting pVPES on silicon surfaces, XPS confirmed three new peaks of N_{1s} at ~402 eV and S_{2p} doublet at ~168.5 eV and ~167.2 eV, corresponding to –C—N, –S—O and –S═O bonds in the pyridine and sulfonate groups, which were not observed in bare silicon and initiator grafted silicon surface (Fig. S5). pVPES brushes also exhibited dynamic surface wettability in response to dual stimuli of salt and pH, as evidenced by contact angles of 43.1°, 36.7°, and 35.9° in water, saline (0.1 M), and basic solutions (0.1 M), respectively. Further i*n situ* friction tests on pVPES brushes exhibited a switchable friction ↔ lubrication behavior, i.e., water-treated pVPES brushes showed a certain degree of surface friction due to the collapsed chain conformations (μ=~3.00), while NaOH/saline-treated pVPES brushes with stretching conformations exhibited super surface lubrication (μ=~0.01), confirming the anti-polyelectrolyte effect of pVPES brushes.

We conducted additional experiments to measure contact angles and friction coefficients of pVPES brushes as treated by different salt solutions of different concentrations, including NaCl solutions (0 ~ 6.1 M), anionic sodium salts (1.0 M; SO_4^{2-}, Cl^-, NO_3^-, and Br^-), and cationic chlorine salts (K^+, Na^+, Mg^{2+}, and Ca^{2+}). In Fig. R1a, as a control, water contact angle was 43.1° on pVPES brushes. However, when switching pure water to salt solutions with different concentrations from 0.5 M to 6.1 M, contact angle of pVPES brushes decreased to 34.5°-36.1°. In parallel, pVPES brushes as treated by different anionic sodium solutions at the same concentration of 1.0 M exhibited a decreased order of contact angles from SO_4^{2-} treated pVPES brushes (~40.0°), Cl^- treated pVPES brushes (~35.1°), NO_3^- treated pVPES brushes (~35.0°), to Br^-treated pVPES brushes (~34.5°). Differently, different cationic chloride-treated pVPES brushes displayed almost same contact angles of ~35.1°. These results indicate that the surface wettability of zwitterionic brushes is more sensitive to Hofmeister anions than to Kosmotrope cations [31,32]. Next, we examined the salt-dependent surface friction behavior of pVPES brushes in pure water, NaCl solutions with different concentrations (0.05–6.1 M), and different salt solutions of anionic sodium salts (1.0 M; SO_4^{2-}, Cl^-, NO_3^-, and Br^-), and cationic chlorine salts (K^+, Na^+, Mg^{2+}, and Ca^{2+}) (Fig. R1b). Specifically, the friction coefficient of pVPES brushes in water was as high as ~3.0, but this value was significantly reduced to ~0.015 when pVPES brushes were treated with NaCl solutions of ≥ 0.53 M, probably because the conformation change of pVPES chains from a collapsed state to a stretching state leads to a smoother surface of pVPES brushes. Similar to contact angles, the friction coefficient of pVPES brushes as treated by salt solutions containing SO_4^{2-}, Cl^-, NO_3^-, and Br^- anions were ~3.6, ~0.05, ~0.03, and ~0.02, respectively, showing a decreased order of interfacial frictions in SO_4^{2-} > Cl^- > NO_3^- > Br^- solutions. Differently, different cation-treated pVPES brushes possessed an increased order of Na^+ (~0.13) < K^+ (~0.14) < Ca^{2+} (~0.18) < Mg^{2+} (~0.23). Particularly, monovalent ions of Na^+ (~0.13) and K^+ (~0.14) presented much lower friction coefficients than divalent Ca^{2+} (~0.18) and Mg^{2+} (~0.23), probably due to a larger amount of monovalent ions for binding to polymer chains. Such ion-dependent anti-polyelectrolyte effect on contact angles and friction coefficients of pVPES brushes was also observed for other zwitterionic polymer brushes of pVBIPS, pSBMA, and pDVBABS in our previous works [33]. Considering the fact that pVPES brushes possess high surface hydration and low friction in salt solutions that are critical for antifouling surfaces, we further examined the surface resistance of pVPES brushes (~26 nm thickness) to both undiluted human blood serum/plasma and bacteria. SPR results showed that upon treating with 0.1 M NaCl, pVPES brushes can retain ultralow fouling level (<0.3 ng/cm^2) in undiluted blood plasma and serum up to 90-min (Fig. S7). Bacteria assays further confirmed that salt-treated pVPES brushes by 0.1 M NaCl resisted 80% colonization of *E. coli* and *S. aureus* at a level lower than ~1.0×10^5 cells/cm^2 up to 24 h, while alkaline-treated pVPES by 0.1 M NaOH enabled to not only kill ~65% of living bacteria in solution, but also release ~70% of dead bacteria from the brushes.

To better test the allochroic property of pVPES, we further synthesized three-dimensional pVPES-SiO_2 nanoparticles (NPs) by surface-initiated atom transfer radical polymerization (SI-ATRP). TEM images of pVPES-SiO_2 NPs clearly showed spherical shapes with average diameter of ~280 nm (Fig. 2d). The grafting of pVPES on the surface of SiO_2 presented typical core–shell structure (200 nm of SiO_2 core and 40 nm of pVPES shell), as confirmed by the well distribution of C, N, and S elements in EDX mapping (Fig. S8), grafted polymer entanglements in the interstitial areas between NPs in TEM images (Fig. S8a), distinct migrated weight loss at ~200 °C pVPES-SiO_2 NPs (Fig. S8b), and the co-existence of ~1670, ~1457, and ~1172 cm^{-1} peaks corresponding to aromatic, pyridine, and sulfonate groups by FTIR spectra (Fig. S8c). pVPES-SiO_2 NPs in aqueous solution displayed reversible and rapid color changes in response to salt and pH stimuli. Specifically, pVPES-SiO_2 NPs showed a fast color change within seconds from milky color in deionized water, to green by adding 0.1 M NaOH to water solution, and to colorless by adding 0.1 M HCl to neutralize acid solution (Movie S1). Similar reversible color change from 0.1 M NaOH at pH = 13 to 0.1 M HCl at pH = 1 was also observed. Such salt- and pH-responsive color changes of pVPES-SiO_2 NPs were stemmed from the two zwitterionic-induced effects of (i) internal charge transfer between different states of VPES moieties and (ii) anti-polyelectrolyte conformational change of pVPES between the collapsed and stretched states. Different from pVPES brush and its surface-based applications, coating of pVPES on SiO_2 nanoparticles allows to create pH-responsive nanoparticles for different solution-based applications (e.g., tumor detection, cell targeting, pH probes).

Furthermore, pVPES-based microgels and hydrogels were also synthesized for studying their structural-independent allochroic property. First, p(VPES-*co*-NIPAM) (PVN) microgels were prepared via a radical polymerization and stabilized by N,N′-methy lenebisacrylamide (MBAA) crosslinking, and their structural and physicochemical properties were characterized by TEM images, SEM-EDX mapping, TG and DSC analysis, and FTIR spectra

[34–36] (Fig. S9). Copolymerization of NIPAM with VPES in microgels allows to introduce additional thermo-responsive color change. Evidently, PVN microgel solution enabled to change its color from colorless in water at 25 °C, to green in 0.1 M NaOH at 25 °C, to colorless again in 0.1 M HCl at 25 °C, to transparent in 0.1 M NaCl at 25 °C and swelling state, and to whiten at 60 °C (Fig. 2e & Movie S2). While pVPES-induced color-change mechanism still holds true for PVN microgels, additional pNIPAM contribution to the color change of PVN microgels should be considered. Given a well-known fact that temperature-responsive pNIPAM undergoes significant volume change and phase separation from a hydrophilic, swelling state below LCST to a hydrophobic, collapsed state above LCST, DLS results showed that PVN microgels changed their hydrodiameters from ~320 to ~600 nm as temperature increased from 25 to 60 °C. Such temperature-induced structural change would further enhance pH- or salt-induced color changes (Fig. 2f), because microgels in the collapsed state had a higher refractive index than in the swollen state due to the expelling of water at higher temperatures, so that the increased refractive index contrast between the collapsed microgel and surrounding water enhances the brightness of the structure color.

As compared to microgels with (sub)micro sizes, PVN hydrogels also exhibited pH- and salt-induced color changes, though macroscopic optical property is far more challenging to achieve. Due to hierarchical network structure formed by zwitterionic-induced conformational transition and thermo-induced microphase separation, it can be seen clearly in Fig. 2g that PVN hydrogels on the top of University of Akron logo experienced reversible color changes between transparent in water at 4 °C with optical transmittance of ~95%, dark green in NaOH of 1.0 M with ~57% transmittance, colorless in HCl of 1.0 M with ~92% transmittance, colorless in NaCl of 1.0 M with ~97% transmittance, and opaque in water at elevated temperature of 60 °C, again demonstrating that the increase of temperature above LCST of pNIPAM leads to microphase separation that largely reduces optical transmittance.

Applications of allochroic polyzwitterions as smart devices

Upon demonstrating the allochroic property of monomeric and polymorphic VPES, we managed to transform VPES or pVPES into different devices for environmental and biological applications. As a first example, we used VPES monomers as highly sensitive colorimetric probes for the detection and identification of environmental pollutants. Design of colorimetric VPES array is based on its pH-induced color changes when interacting with different toxic organic amines (TEMED, TEA, EDPA, PMDTA, EDA, DETA, AYA, Me_6, DMAEMA, EOA, DMAPAA, DMAP, DEA, and DBA) [37,38]. To achieve this goal, VPES solution (0.01 g/mL) was first preactivated at a zwitterionic colorless state, followed by adding 10 mg/mL of different toxic amines. Visual inspection in Fig. 3a showed an immediate color change from colorless to green to different extents within seconds in response to different toxics. Further *in-situ* UV–vis spectra confirmed that addition of toxic amines to VPES solution caused a consistent color change from colorless to green with a prominent time-dependent enhancement at the absorption maximum of ~612 nm (Fig. S10). Specifically, all of as-prepared VPES solutions (0.005 g/mL) exhibited no color and no distinct transmittance peak at the range of visible light (400–760 nm). Upon adding organic amines (DMAEMA, TEMED, TEA, EDPA, PMDTA, EDA, DETA, AYA, Me_6, EOA, DMAPAA, DMAP, DEA, and DBA) into VPES solutions, all of binary mixtures presented different optical transmittance (37.5–81%) and color changes from colorless to varying degrees of green. Further, optical transmittance (i.e., maximum absorption peak) and color state (i.e., green) of VPES in the presence of toxic amines remained almost unchanged within 30 min, indicating that VPES and toxic amines can form a stable suspension at the deprotonated state. Such major adsorption is caused by the intramolecular charge transfer at the acceptor site of pyridyl groups upon coordination with solvated hydroxide ions. Different extents of colorimetric transmittance are likely attributed to the binding formation and affinity between VPES and amines. DMAEMA with the lowest pK_a of 7.5 are not sufficiently basic to deprotonate VPES, thus displaying a low transmittance difference of <17%. Differently, DMAP, EDPA, and Me_6 with more electron-donating substituents (e.g., pyridyl, isopropyl, and *tert*-butyl) have the higher pK_a values to 8.79–11.39, thus leading to the increased transmittance difference of 37.5–81%. Further, optical transmittance (i.e., maximum absorption peak) and color state (i.e., green) of VPES in the presence of toxic amines remained almost unchanged within 30 min, indicating that VPES and toxic amines can form a stable suspension at the deprotonated state.

We further applied PVN hydrogels to sandwich-structured smart windows with high-contrast, reversible, color switching between transparent and green states in the response to pH [39,40]. A sandwich structure was used by placing a PVN hydrogel layer in between the two glasses, where the inert electrodes are embedded on both glass sides (Fig. 3b). Upon applying voltage, the oxygen evolution reaction on the anode occurs to produce proton and oxygen gas ($2H_2O \rightarrow O_2(g) + 4H^+(aq) + 4e^-$), leading to a local pH decrease, while hydrogen evolution reaction at the cathode yields hydrogen gas and hydroxide ions, resulting in a local pH increase ($2H_2O + 2e^- \rightarrow H_2(g) + 2OH^-$). Consequently, such localized pH changes near hydrogel/electrode interfaces induced the color change of PVN hydrogels from colorless to cyan. Additionally, thermo-responsive pNIPAM in PVN hydrogels can further tune the optimal transmittance for energy saving. As shown in Fig. 3c, we compared optimal transmittance variations of the same windows between open and closed circuits at different temperatures. At open circuit and 20 °C, the PVN window (0.3 ~ 2.5 μm of wavelength, hydrogel thickness of 1 mm) exhibited as high as 86.5% of luminous transmittance (T_{lum}), 81.3% of infrared transmittance (T_{IR}), and 85.7% of solar transmittance, respectively (red line), making it almost identical to that of the pristine window with high transparency. After short circuit for 30 s, the PVN window immediately changed its color from colorless to green, in accompany with a significant transmittance decrease to 14.3% at 612 nm (green line). Increase of temperature to 50 °C also led to a rapid transmittance reduction of PVN windows to 10.7% of T_{lum} and 21.3% of T_{IR}, respectively. Visual inspection of a PVN smart window on the top of University of Akron logo exhibited similar

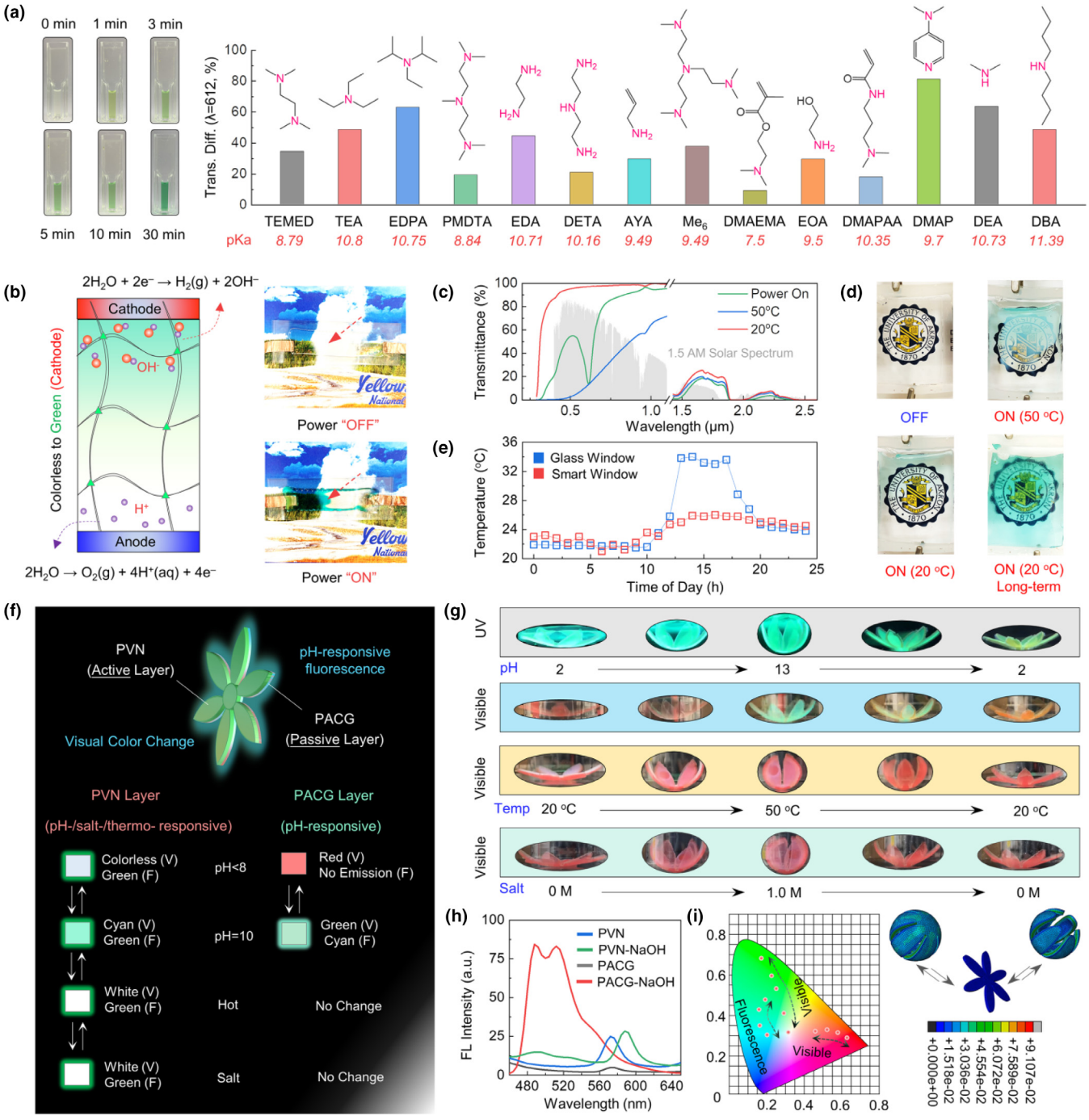

FIGURE 3

Smart zwitterionic, allochroic devices. (a) Optical transmittance response of VPES solution in the presence of different organic amines (TEMED, TEA, EDPA, PMDTA, EDA, DETA, AYA, Me_6, DMAEMA, EOA, DMAPAA, DMAP, DEA, and DBA). The column bars represent the time-dependent UV transmittance ratios ((T_1-T_{30})/T_{30} at λ = 612 nm) of VPES solution at 1 min and 30 min after the addition of the amines. (b) Schematic of sandwich-like structure and electrochromic mechanism of PVN smart window, with real-time images for demonstrating visual change in transmittance from ~95% to ~15% and color from colorless to green. (c) UV–vis-NIR transmittance of PVN window upon exposure to different conditions of 20 °C (Red), 50 °C (Blue), and a voltage of 9.0 V (Green), respectively. Gray shadow area represents the spectrum of sunlight in the UV–vis-NIR range for comparison. (d) Digital photographs of a PVN smart window to show both transparency and color changes from a complete transparency at an open circuit, to semi-transparency and light green at 20 °C and a close circuit (5 s), to opaque and dark green at 20 °C and a close circuit for 1.0 h, and to milky and green at 50 °C and a close circuit (1 min). (e) Time-dependent back-air temperatures for regular glass window and PVN smart window on a sunny day at Akron. Smart window exhibits a very small temperature fluctuation as compared to regular glass window. (f) Bilayer design and working principle of a hydrogel actuator, consisting of a pH/temperature/salt responsive PVN layer and a pH-responsive PACG layer, for achieving both color and shape changes. (g) Amphibious self-actuation behaviors of a petaloid-like actuator made of bilayer PVN/PACG hydrogel to resemble the closing or blossoming of a real flower with color changes under different thermo-/pH-/salt- stimuli. Movies S3-8 were also recorded for the entire actuation processes. (h) Fluorescence spectra (λ_{ex} = 365 nm) of individual PVN and PACG hydrogel layer in different NaOH solutions of pH 2 and 13. (i) Chromaticity coordinates and finite element modeling of PVN/PACG hydrogel actuator to show color change pathways in response to pH (2–13) and temperature (20 ~ 50 °C).

color changes from the colorless at open circuit and 20 °C, to semi-transparency and light green at 20 °C and a close circuit (5 s), to opaque and dark green at 20 °C and a close circuit (1.0 h), and to milky and green at 50 °C and a close circuit (1 min). (Fig. 3d). Equally important, the PVN windows were tested outside on a sunny day at University of Akron, in comparison with the conventional windows. As shown in Fig. 3e, conventional windows with a complete transparency experienced a typical diurnal temperature variation between the highest temperature of 33.2–34.0 °C at noon and the lowest temperature of 21.5–24.7 °C at night. In sharp contrast, the PVN window only experienced a very small temperature change between 21.9 and 26.0 °C, as a result of a highly tunable transmittance between the complete transparent state and the opaque state. Such sunlight-induced transmittance change is attributed to sunlight-induced temperature change to cause the phase separation of thermo-responsive pNIPAM in the PVN hydrogels, which eventually result in a difference of refractive index for the blockage or transmission of incident light.

We also developed a bilayer hydrogel actuator, consisting of an active/optical PVN layer and a passive/fluorescent PAAm-PTCG (PACG) layer, for achieving both color-changing and complex shape-deformation functions [41–45]. Each layer was carefully designed to achieve different functions, i.e., PVN layer enables to undergo both volume and color changes simultaneously in response to pH, temperature, and salt, while PACG layer possesses pH-demanding on/off fluorescence, but is inert for actuation (no shrinking and swelling) at alkali/acidic conditions (Fig. 3f). To test the multiple stimuli-responsive actuation, we prepared a petaloid-like actuator made of PVN/PACG bilayer hydrogel, allowing to resemble the closing or blossoming of a real flower with color changes under different stimuli (Movies S3-8). Evidently, after immersing an open, flat petaloid actuator into a 0.1 M NaOH solution of pH 13, its outer petals immediately started to fold into a closed structure (Fig. 3g), accompanied by multi-fluorescence change of (i) the PACG layer from no fluorescence to bright green at ~480 and ~512 nm and (ii) the PVN layer with redshifting from ~570 nm to ~582 nm due to the electron withdrawing effect from styryl and conjugated pyridyl moieties [46] (Fig. 3h). Such alkaline-induced petaloid closing was fully reversible to a blooming-like structure with color changes of the PACG layer to red fluorescence and the PVN layer to colorless by adjusting pH to neutral or acidic conditions. Similarly, the petaloid folding and unfolding processes in salt- and thermo-responsive conditions were always found to be highly reversible with no noticeable degradation between 60 °C and 4 °C and between 1.0 M to 0 M of NaCl solution for 10 cycles. At the same time, petaloid actuators experienced reversible, visible color changes between colorless at 4 °C and white at 50 °C and between white in water and colorless in a 1.0 M of NaCl solution, both due to thermal-/salt-induced phase separation of PVN layer. Finally, we presented both visible and fluorescence color change pathways of PVN and PACG layers in the chromaticity diagram in response to pH, temperature, and salt (Fig. 3i). It can be seen that a reversible fluorescence change of both layers was observed between cyan (0.20, 0.30) at pH 2.0 and green (0.19, 0.47) at pH 13, while visible color was changed from (0.17, 0.67) to (0.32, 0.31) for PVN layer under pH and thermal stimuli and from (0.46, 0.32) to (0.63, 0.28) for PACG layer under pH stimuli. In parallel, finite element modeling confirmed the experimental observation of synchronous deformation and discoloration under solvated thermal stimuli [47,48] (Movie S9).

Long-term subcutaneous implantation and monitoring of allochroic hydrogels in mice

Major function and applications of zwitterionic materials are mostly limited to their biocompatibility due to their highly hydrophilic and antifouling properties [49,50], zwitterionic materials with allochroic property have not been reported yet [51]. Here, after demonstrating the zwitterion-empowered allochroic and antifouling properties of pVPES-based polymers and their applications *in vitro*, we continued to investigate how pVPES-based hydrogels can be synchronously used as not only wound dressing upon implantation in mice, but also diagnostic bioimaging to monitor and respond local pH/ion changes during wound healing process (Fig. 4a). Specifically, we used a murine skin wound model to construct both chronic (red mice) and acute (blue mice) wounds, then applied two-layer PVN hydrogel patches to these full-thickness cutaneous wounds in mice, with particular attention to wound healing and monitoring in response to local pH and ionic concentration changes around or underneath wounds. Given that chronic wounds are found to reside at predominately alkaline pH of 7.0–9.0, while acute wounds have a more neural pH [52], PVN hydrogel patch is designed to be pH-sensitive by constructing the two layers of an alkaline-activated zwitterionic PVN hydrogel disk (green) and a highly breathable adhesive gauze cloth (transparent). Before *in vivo* wound healing and monitoring tests, we first confirmed that (i) PVN patches had almost no cell cytotoxicity, as evidenced by cell viability of ~99.0% in PVN patches, ~99.5% in Tegaderm films, and ~98.7% in polystyrene (PS)-Nunclon (Fig. S11) and (ii) PVN patches exhibited pH-responsive color changes, i.e., the activated PVN patches enabled to retain their green color in interstitial fluids of pH = 8.0, but gradually changed to colorless in acidic interstitial fluids of pH = 6 (Fig. 4b).

Upon applying PVN patches to both chronic and acute wounds in BALB/c mice for 2 weeks, visual inspection of wound bed closure and the corresponding mimetic trace revealed that both PVN-treated chronic and acute wounds recovered much faster with better skin appearance than the Tegaderm-treated control groups (Fig. 4c & S12). During 2-week treatments, wound closure rates of PVN-treated chronic wounds were higher than those of PVN-treated acute wounds at all treatment times (days 3, 7, 10, and 14), among which the final wound closure rates at day 14 were > 99% and ~95% for PVN-treated chronic and acute wounds, respectively. Particularly, the PVN-treated chronic wounds were completely healed and almost scar-less at day 14, as compared to some residual wound areas in PVN-treated acute wounds. Further, as shown in Fig. 4d & S13 by H&E staining results on day 7, PVN-treated chronic and acute wounds exhibited the high regeneration of re-epithelialization and granulation tissue, as evidenced by the formation of many hair follicles and blood vessels (red arrows) and the shorter epidermal gaps (2.20 ± 0.25 mm and 1.77 ± 0.20 μm), in sharp contrast to Tegaderm-treated wounds with more inflammatory cells, the

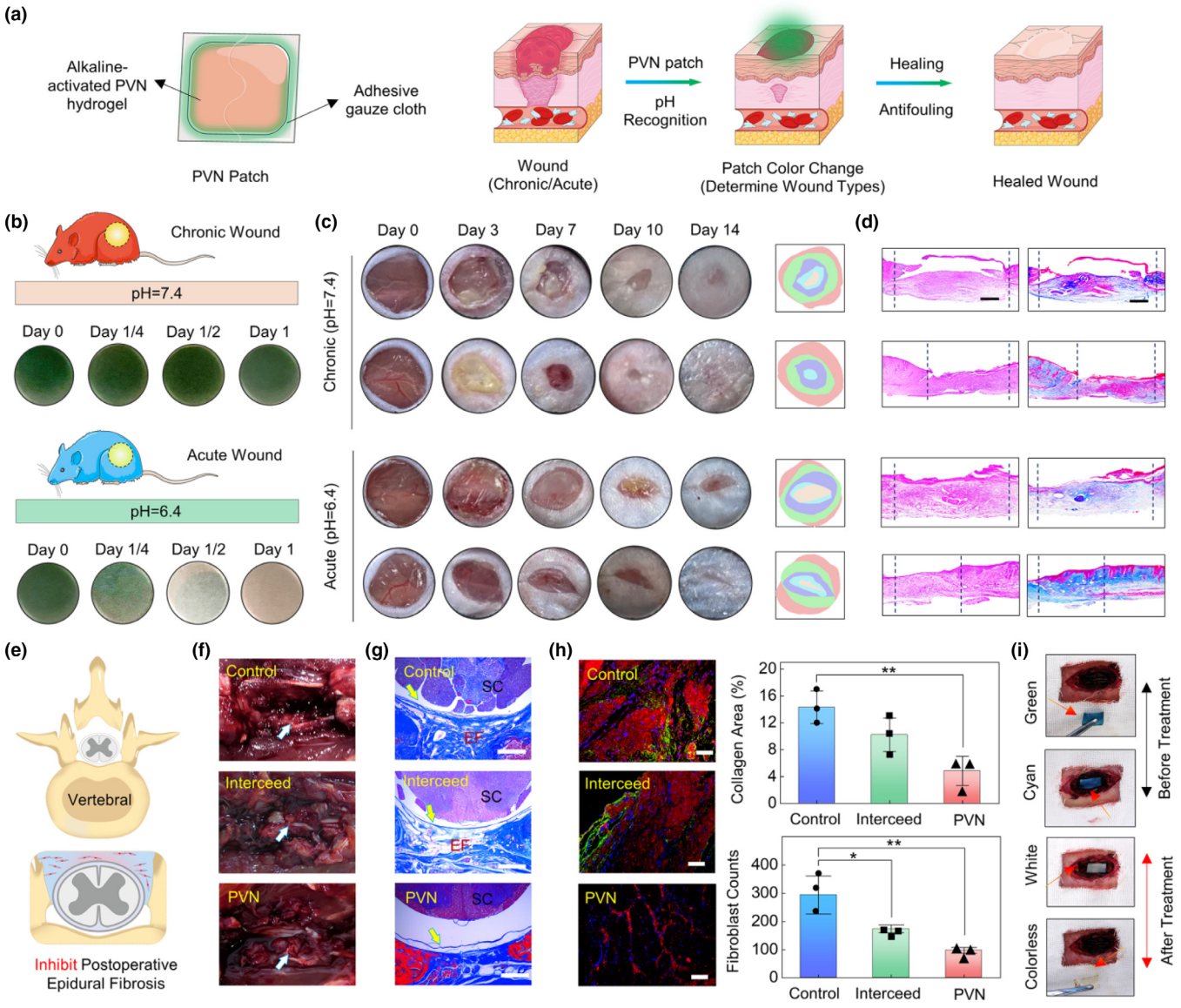

FIGURE 4

Zwitterionic PVN hydrogels present wound healing and monitoring of long-term subcutaneous implantation in mice. (a) Schematic of a PVN hydrogel patch and its synchronous functions for wound healing and diagnostic imaging in mice in response to local pH/ion changes. (b) Time-dependent diagnostic images of activated PVN hydrogel patches to shown color changes for both chronic and acute wounds in mice. (c) Macroscopic wound healing process of chronic and acute wounds at different time intervals (day 0 ~ 14) after treating with activated PVN hydrogel patches (bottom) and Tegaderm films (Top), as well as the corresponding wound closure traces on day 14. (d) Hematoxylin and Eosin staining (left) and Masson's Trichrome staining (right) of wound tissues from activated PVN hydrogel- and Tegaderm films-treated groups on day 7 post-operation. Scale bar: 500 μm. (e) Illustration of PVN hydrogel patch to prevent long-term epidural fibrosis and adhesion on wounds of Male Sprague-Dawley rats. (f) Macroscopic surgical opening (white arrows indicate the epidural scar tissues) and (g) Masson-stained images mice (SC: spinal cord, EF: epidural fibrosis; Scale bar: 500 μm) of laminectomy sites in mice upon no treatment (control), treating with Interceed, and PVN hydrogels at 25 weeks. (h) Immunofluorescence staining of COL I and III distributions and the corresponding statistics of collagen area and fibroblast counts in epidural area for the control, Interceed films-treated, and PVN hydrogels-treated groups at 25 weeks. Scale bar: 50 μm. *P < 0.05 and **P < 0.01. (i) Visible color change from green to colorless for activated PVN hydrogels being treated with acute wounds in mice.

looser subcutaneous tissue, and the larger epidermal gap of 3.0 9 ± 0.20 mm. Again, PVN-treated chronic wounds had far thicker and more continuous epithelial layers of granulation across the entire wound gap than PVN-treated acute wounds. Consistently, MTS results showed that the PVN-treated acute wounds accumulated more collagens and thick collagen fibers on wound sites than other wounds (Fig. 4d & S13; right). Additionally, collagen fibers in PVN-treated chronic wounds were well organized and aligned with similar morphology to normal dermal skin, in agreement with completely healed wounds without no obvious sign of inflammation or scars near the wound areas. Taken together, PVN patches not only accelerate wound closure for both chronic and acute wounds with significant differences from control groups ($P < 0.05$), but also distinguish chronic wounds - from acute wounds.

More importantly, prevention of undesirable epidural fibrosis upon subcutaneous implantation in rats is critical for reducing or eliminating the foreign body reaction. We continued to examine

in vivo fibrous scar resistance of PVN hydrogels upon subcutaneous implantation of them on the back of immunocompetent Sprague-Dawley rats for up to 6 months (Fig. 4e). Dura mater tissues in contact with alkaline-activated PVN hydrogels were collected from rats at 25 weeks to evaluate potential fibrous scar formation. The results were also compared with those tissues collected from rats that were implanted with commercial Interceed films (positive control) and from rats that did not have any surgery (negative control). After the 25-week implantation, few cells were accumulated at the interface between skin tissues and PVN hydrogels, as indicated by less basophilic discoloration (Fig. 4f). PVN-treated rats also had significantly less fibroblast infiltration and the formation of fibrotic tissue (MRI imaging, Fig. S14). Skin tissues adjacent to PVN hydrogels showed no observable dense fibrous scar formation, indicating no acute inflammatory response. In contrast, upon Interceed implantation, we observed the rapid cell attachment to the skin/Interceed interface, followed by the formation of dense and mature collagenous scar at the 25 weeks. Quantitively, H&E staining results revealed that PVN-treated groups exhibited more smooth fibrous tissue and explicit histological section gaps of 685 ± 100 μm, in sharp contrast to Interceed-treated wounds and control group with more compact subcutaneous tissue and almost indistinguishable gaps (<100 μm) (Fig. S15). Such distinct gaps prevent the secondary nerve compression and subsequent re-lesions of the healed wounds. MT staining, from a different angle, confirmed that the PVN-treated groups exhibited a large reduction in average epidural fibrosis grades of 1.0–2.0, as compared to both control and Interceed-treated wound (Fig. 4g & S16). COL I and III distribution in epidural area showed that PVN-treated wounds enabled to inhibit neovascularization at laminectomy sites by reducing TGF-β1 production via macrophages (Fig. 4h). As compared to both control and Interceed-treated wounds, PVN-treated wounds reduced the average collagen area by 4.87 ± 2.15% and the average fibroblast counts by 97.3 ± 10.2, indicating the formation of a thin peripheral rim of enhancement around the dural sac, but no direct dura adhesion on zwitterionic PVN treated wounds [53]. So, PVN hydrogels reduced epidural fibrosis by inhibiting fibroblast proliferation and extracellular matrix overexpression and deposition via a TGF-β and macrophage expressing pathway. More importantly, activated PVN hydrogels showed visible color change from green, cyan, and white to colorless after extracting from the postoperative wounds, again confirming the acidic pH-induced color changes for acute wounds in laminectomy (Fig. 4i). Overall, our PVN hydrogels provide a proof-of-concept example for realizing both wound healing and monitoring in mice, demonstrating their excellent biocompatibility and allochroism being co-presented in the same zwitterionic materials.

Discussion and outlook

Zwitterionic materials, due to the co-presence of equally cationic and anionic moieties in the same polymer chains, have been well recognized as, but largely limited to, inert materials for their excellent antifouling and biocompatible properties for different bio-applications. Beyond these properties, zwitterionic materials with new allochroic property have not been discovered yet, because the intrinsic incompatibility between hydrophobic allochroic moieties with poor water solubility/high cell toxicity and highly hydrophilic zwitterionic moieties with benign biocompatibility prevents these two distinct properties from co-existing within a single zwitterionic material.

Here, we reported a pure polymeric zwitterion of pVPES, consisting of zwitterionic quaternary ammonium-sulfonate group with chromogenic pyridine-derivative group, to achieve intrinsic, built-in nonfouling and allochroic properties. The resultant pVPES can be further polymerized into different architectures (linear brushes, sphere colloids, microgels, and hydrogels) but still retaining the common pH-responsive allochroic property. Next, pVPES served as a common functional template to copolymerize with different stimuli-responsive polymers for integrating distinct function with allochroic property in different smart pVPES-based devices/materials, including (i) colorimetric array for a rapid detection of different environmental pollutants, (ii) electrochromic smart windows with reversible color and transmittance switching between a transparent, colorless state and an opaque, green state in response to temperature/pH, and (iii) bilayer hydrogel actuators capable for synchronous shape deformation and discoloration in response to pH, temperature, and salt. Finally, pVPES-based hydrogel patches were designed and applied to both full-thickness chronic and acute wounds in mice, in which the hydrogel patches can not only accelerate wound closure for both chronic and acute wounds (e.g., promotion of hair follicle regeneration and prevention of fibrous scar formation), but also distinguish chronic wounds from acute wounds, demonstrating both wound healing and monitoring functions in vivo. This work not only demonstrates a new zwitterionic polymer with un-explored allochroic property and proven applications *in vitro* and *in vivo*, but also provides design principles for zwitterionic, allochroic materials for different bio-optics applications.

Methods

Materials

4-Pyridinylethanesulfonic acid (99%), tetrahydrofuran (>99.9%), sodium hydroxide (97%), formamide (>99%), Monodisperse silicon dioxide nanoparticles (SiO_2 NPs, ~200 nm), 4-vinylbenzyl chloride (90%), acetone, anhydrous ethanol, Gelatin (type A and gel strength ~300 g bloom), N-isopropylacrylamide (NIPAM, 97%), acrylamide (AAm, >99%), 3, 4, 9, 10-perylene tetracarboxylic dianhydride (97%), potassium hydroxide flakes (90%), α-bromoisobutyryl bromide, trifluoroethanol (>99%), PBS buffer, ammonium persulfate (APS, >98%), N, N′-methylenebis(acrylamide) (MBAA, 99%), (3-Aminopropyl)triethoxysilane (APTES, >98%), inorganic salts (e.g., NaCl, Na_2SO_4, NaBr, $NaNO_3$, KCl, CuBr, $MgCl_2$, and $CaCl_2$), amine derivatives (e.g., Tris[2-(dimethylamino)ethyl]amine (Me_6, 97%), N, N, N′, N′-tetramethylethylenediamine (TEMED, 99.5%), triethylamine (TEA, 99%), N, N-diisopropylethylamine (EDPA, 99.5%), N, N, N′, N″, N″-pentamethyldiethylenetriamine (PMDTA, 99%), dimethylamine (DEA, 40wt% aqueous solution), dibutylamine (DBA, 99%), ethylenediamine (EDA, 99.5%), diethylenetriamine (DETA, 99%), allylamine (AYA, 98%), 2-(dimethylamino)ethyl methacrylate (DMAEMA, 98%), N, N-dimethylamino propylacrylamide (DMAPAA, 98%), ethanolamine (EOA, 99%), and 4-dimethylaminopyridine (DMAP, 99.5%)) and acid-base indica-

tors (e.g. litmus, methyl orange, phenolphthalein, anthocyanin, ethyl green, and methyl violet) were purchased from Sigma-Aldrich. Water used in these experiments was purified by a Millipore water purification system with a minimum resistivity of 18.0 MΩ cm. All other reagents were commercially obtained and used as received without any purification.

Synthesis of zwitterion VPES

4-pyridinylethanesulfonic acid (18.72 g, 0.1 mol) and sodium hydroxide (4.0 g, 0.1 mol) were dissolved in 150 mL of formamide solution with magnetic stirring under ambient temperature. Subsequently, 4-vinylbenzyl chloride (15.26 g, 0.1 mol) was added to the flask in a dropwise manner under high-purity nitrogen. The reaction was carried out at ambient temperature and stirred for 72 h, precipitated in acetone, and filtrated to obtain the crude products. Finally, the products were recrystallized with anhydrous ethanol, and the yield of VPES was ~72.3%. ^{13}C NMR (300 MHz, D_2O): δ 166.71, 160.71, 143.53, 138.81, 135.72, 132.31, 129.31, 128.27, 127.09, 115.77, 63.55, 49.62, 30.42. ITMS (m/z): $[M]^+$ calculated for $C_{16}H_{17}NO_3S$, found, 302.32.

Synthesis of fluorescent gelatin (PTCG)

Fluorescent PTCG was synthesized by coupling 3, 4, 9, 10-perylene tetracarboxylic dianhydride and gelatin macromolecules. In brief, 3, 4, 9, 10-perylene tetracarboxylic dianhydride (0.5 g) was dispersed in THF (20 mL) to obtain a clear solution, which was slowly added into 20 mL prefabricated gelatin solution (2 g/mL, 50 °C). After 20 h, THF as an organic phase was removed from the system and KOH (0.5 g) was added to hydrolysis the unreacted anhydride. The raw product was precipitated by gradually dipping 50 mL of 10% HCl solution, centrifuged by 10,000 rpm for 5 min to fully remove the unreacted reagents. After the pH of solution was adjusted to alkaline by gradually adding NaOH, the solution was dialyzed (cut-off M_n = 3500) in water for at least 1 week. The final product was obtained as an amorphous solid by lyophilization. Note that such synthesized gelatin derivatives possess a distinguished pH-responsive fluorescence transition.

VPES-gauged acid-base titration

VPES (0.01 g) was firstly dissolved in 2.00 mL of water to prepare the standard indicator. The VPES as a unique pH indicator was pre-activated by 0.1 M NaOH solution, and gradually adjusted pH to 7 for stand-by use. Titration processes, i.e., "Acid-to-Alkaline" and "Alkaline-to-Acid" were followed by standard procedures.

For example, in a typical ("Acid-to-Alkaline") experiment, 0.1 M HCl aqueous solution (already calibrated) was firstly added into settled 25 mL acid burette, followed by gently rotating the piston so that the tip of the tube was filled with HCl solution without any bubbles. The solution level was adjusted to keep it at "zero" or below a certain scale and took an accurate reading. The alkaline solution with an unknown concentration (10.00 mL) was added into a conical flask containing a small number of indicators (including methyl orange (MO), litmus, phenolphthalein, VPES + MO, and VPES + Litmus). Small volumes of titrant were then dropwise added to the analyte until the indicator changed color in reaction to the titrant saturation threshold. The changed color should maintain stable at least 15 s, representing arrival of the titration endpoint. The practical volume of adopted HCl solution was recorded and repeat the titration process at least three times to obtain the average volume.

Visualized detection of toxic organic amines

To avoid the structural interferes, different toxic organic amines with certain alkalinity (pK_a > 7) were selected to demonstrate visualized detection one-by-one, including TEMED, TEA, EDPA, PMDTA, EDA, DETA, AYA, Me_6, DMAEMA, EOA, DMAPAA, DMAP, DEA, and DBA, respectively. For instance, 10 mg TEMED (liquid) was added into 1 mL of VPES solution (0.005 g/mL), the color change processes were directly recorded by a digital camera. Simultaneously, each sample was placed into the cavity to obtain UV–vis spectrum at regular reaction intervals (1, 3, 5, 10, and 30 min).

Fabrication of pVPES brushes grafted SPR chip

SPR chip was firstly rinsed with ethanol, acetone and water sequentially, later treated under UV ozone for 20 min, washed by DI-water and finally air-dried. Before surface initiated (SI)-ATRP reaction, an initiator self-assembled monolayer (SAM) was first anchored onto the SPR chips by soaking SPR chips into 1 mM ω-mercaptoundecyl bromoisobutyrate (initiator) ethanol solution at room temperature overnight due to the unique strong interaction between sulfhydryl group and Au atoms, followed by ethanol flush and air-dried.

Surface-initiated atom transfer radical polymerization (SI-ATRP) enabled to establish a desirable atomic scale precision in surface topology and chemistry. Under the nitrogen atmosphere, a tube containing VPES (0.5 g), Me_6 (20 mg), and degassed CF_3CH_2OH/saline (0.1 M NaCl) (1:1, v%) solution was transferred to another tube containing SPR gold chip coated with immobilized initiators and CuBr (12.5 mg) and then SI-ATRP reaction was immediately started at room temperature. The reaction was stopped by exposure to air after the controlled reaction time (0 ~ 24 h). To remove unreacted monomers or unbounded polymers, the chips were soaked in PBS buffer overnight.

Fabrication of pVPES brushes grafted silicon dioxide nanoparticles

SiO_2 NPs were firstly dispersed in 40 mL ethanol with 50 μL ammonium hydroxide after being degassed for ~15 min under a high-purity nitrogen atmosphere. When the temperature increased to 60 °C, APTES (0.4 mL, 1.7 mmol) was added dropwise to the mixture at 300 rpm. The APTES-modified SiO_2 NPs (SiO_2-NH_2) were obtained at 8000 rpm centrifugation after 12 h reaction. The solid ATRP initiators, SiO_2-Br NPs were obtained by reaction between α-bromoisobutyryl bromide (0.25 mL) with SiO_2-NH_2 (4.0 g).

The pVPES-SiO_2 NPs were also synthesized by the SI-ATRP method. Briefly, 0.8 g of SiO_2-Br NPs and 2.0 g VPES were dissolved in 4.0 mL of CF_3CH_2OH/saline (1.0 M NaCl) mixture (1:1, v%), subsequently combined with 30 μL of Me_6 and 5 mg of CuBr under a high-purity nitrogen environment. pVPES-SiO_2 NPs with various brush thicknesses could be obtained by regulat-

ing the reaction time, e.g., 4, 6, 12, and 24 h. The obtained raw products were then washed at least 3 times with NaCl solution (3.0 M) to fully remove unreacted monomers, collected by centrifugation, and eventually dried for standby application.

Preparation of poly(VPES-co-NIPAM) (PVN) microgels and hydrogels

The PVN microgels were synthesized by the typical dispersion polymerization. Reactants consisting of NIPAM (0.4 g), VPES (0.1 g), and 50 mL deionized water were all mixed into a round-bottom flask with stirring (400 rpm) and pre-deoxygenated with N_2 flow for 30 min. Subsequently, the initiator potassium persulfate (APS; 25 mg) and cross-linker MBAA (25 mg) were added into mixture. The polymerization was initiated when heated to 75 °C under the protection of nitrogen atmosphere, and the reaction was terminated by exposure to air after 5 h. The microgels were purified in a dialysis cassette (cut-off M_n: 8–14 kDa, Thermo Scientific) with deionized water for at least one week.

Similarly, monomers (NIPAM (900 mg) and VPES (100 mg)), APS (10 mg), MBAA (6 mg) were dissolved in 6 mL of deionized water to obtain a transparent solution. The resultant solution was then purged by N_2 for 10 min to fully remove the oxygen inside, subsequently, TEMED (4 μL) was added and then gently injected into a mold prepared by separating two glass slides with a 1.0 mm Teflon spacer. After polymerization at 4 °C for 12 h, the PVN hydrogel was prepared for stand-by use.

To demonstrate the unique soft actuator, PVN/PACG hydrogel with bilayer structures was further synthesized, which showed dual optical/fluorescence color change under the repeat pH switch. The obtained PVN hydrogel was firstly put into the pre-set mold separated two glass slides with a 2.0 mm Teflon spacer. Subsequently, AAm (2 M) precursor solution containing PTCG (20 mg), MBAA (0.05 wt% of AAm), and APS (9 mg, 0.04 mmol), TEMED (2 μL) was quickly injected into the mold at 4 °C. The bilayer structured hydrogel was formed for 2 h, taken out, and immersed in 0.1 M PBS solution to remove any unreacted monomers.

Finite element modelling method

The results presented in this manuscript were calculated by using Abaqus 6.13. Bilayer-structured hydrogels in this simulation were set as Neo-Hookean hyperelastic materials, the shear modulus and bulk modulus were set as "1" and "10–5". The slow volume change of hydrogels was formulated by a quasi-static process and acquired in the simulation by multiplying the total volume change with the step length (by using solvated thermal stimuli). 8-node biquadratic axisymmetric quadrilateral, hybrid reduced integration element (CAX8RH) were used in the simulation.

Density functional theory

All the calculations in this work were performed by using Gaussian 03 program package at PBE0 functional with 6–31++G(d, p) basis set. HOMO-LUMO surfaces calculation have analyzed based on the optimized geometry in water.

Characterization of allochroic monomers and polymers

^{1}H NMR spectra of VPES and its alkaline-treated derivative were measured on Bruker Avance AMX-400 Spectrometer in D_2O using tetramethylsilane as the internal reference. The structural morphologies of pVPES-SiO_2 NPs and PVN microgels were measured by transmission electron microscopy (TEM, JEOL JEM-100CX-II) equipped with an EDS detector. Briefly, the obtained samples were dispersed ultrasonically in ethanol, subsequently dipped on a carbon-coated copper grid, and fully dried before observation. The chemical composition of pVPES modified surfaces was characterized by X-ray photoelectron spectroscopy (XPS) (Kratos Analytical), while the brush roughness and morphology were detected by an atomic force microscope (AFM, Bruker Dimension) at the frequency of 170–180 kHz and the RMS roughness was obtained by Nano scope analysis. Water contact angle (CA) was conducted on an OCA 15EC Video-based Optical Contact Angle Measuring System (Eastern-Dataphy), testing conditions include water, NaOH (0.1 M), and saline (0.1 M). SPR tests on pVPES brushes modified SPR chips (~26 nm of thickness) were conducted by using a home-made 4-channel sensor. Dynamic light scattering (DLS, NanoBrook-Omni) using a He-Ne (633 nm) laser was performed at different required temperatures, after the applied concentration of NPs or microgels was diluted. UV–vis absorption spectra were recorded by virtue of a UV–vis spectrophotometer (UV1800) provided by Shimadzu Co., Ltd. Fourier transform infrared spectroscopic measurements were conducted by using a Nicolet-6700 with resolution of 4 cm^{-1} and 32 scans. The weight loss of pVPES-SiO_2 NPs and PVN microgels was characterized by thermogravimetric analysis (TGA, Q5000-IR) from 25 to 600 °C at a heating rate of 10 °C/min under N_2 atmosphere. Differential scanning calorimetry (DSC) was recorded by a Discovery DSC250 (TA Instruments) under a high-purify N_2 atmosphere. Typically, a small amount of PVN microgels was encapsulated in a hermetic Aluminum pan with a cyclic heat-cool-heat mode and controlled heating rate of 10 °C /min. As for surface friction tests, the pVPES modified silicon wafers were measured on a Universal Micro-Tribometer (UMT-2, CETR) equipped with a poly(dimethylsiloxane) hemisphere (6 mm of diameter). In particular, the wetting conditions can be adjusted including water, NaOH (0.1 M), and saline (0.1 M).

Cell and bacterial biocompatibility

For cell cytotoxicity, the as-prepared PVN hydrogel patches, Tegaderm films, and polystyrene (PS)-Nunclon were sterilized with UV light for 1.0 h and subsequently immersed into the fresh medium to reach swelling equilibrium. The sterile specimens were then placed into a 24-well plate and L929 cells were seed on the upper surfaces for 1–3 days. After 3-day coculture, the cells were fixed and stained with Calcein AM/PI and imaged by using an inverted fluorescence microscope (Zeiss, Germany).

Secondly, typical bacterial strains (*E. coli* and *S. aureus*) were applied to challenge the antifouling zwitterionic surfaces (pVPES brushes) in liquid media. Specifically, the selected bacterial strain was incubated overnight on agar plates to obtain single bacterial colony, followed by inoculated in the corresponding liquid medium (i.e., Luria-Bertani (LB) for *E. coli* while using Trypticase soy (TS) for *S. aureus*) and further cultured for another 12 h/ 6 h at 37 °C. Subsequently, the resultant high-density bacterial solution was immediately diluted to a pristine cocultured bacterial solution with an OD value of 0.1 (*E. coli*) or 0.05 (*S. aureus*). The pre-

sterilized specimens (exposure to UV light for an hour) were placed into a 6-well plate and added a certain amount of the configured diluted bacterial solutions. After cocultured in shaking conditions (37 °C, 120 rpm) for another 24 h or 12 h, the cocultured chips were taken out and then stained by diluted LIVE/DEAD Backlight Viability Kit solutions (Thermo Fisher Scientific Inc., NY) for 20 min. The specific live/dead rate and antifouling performance of pVPES brushes were observed by a fluorescence microscope (Echo Revolve R4) with a 20×/10 × lens. All specimens were randomly selected for imaging while the statistical analysis was performed by using the software ImageJ.

In vivo full thickness wound healing assay

In vivo full thickness wound healing assay of PVN hydrogel was carried out from the Laboratory Animals Center at Wenzhou Medical University. 18 Male BALB/c mice (5–6 weeks) were randomly divided into three groups (6 replicates per group): blank, acute, and infected, and created two identical circular full-thickness wounds (d = 6 mm) per mouse. Specifically, (i) the acute group created the wound directly on the back of the mouse and put on the PVN hydrogel dressings; (ii) the infected group was to pre-infect the wounds with *S. aureus* and made it inflamed and pus before applying the hydrogel dressing; (iii) Mice with bare wounds served as controls. Healing progresses of the wounds were captured by a digital camera on day 0, day 3, day 7, day 10, and day 14 postoperatively, and changed the hydrogel dressings after observation. At specific time intervals (on day 7), the skin tissue was excised for pathological analysis of wound. After hematoxylin and eosin (H&E) staining and Masson's Trichrome (MT) staining, the histological images were observed by optical microscope. The care and experiments of animals were approved by the Ethics Committee of Wenzhou Medical University and strictly followed with International Code of Ethics and the National Institutes of Health (No. wydw20180043).

Establishment and intervention of designed animal model

A rat laminectomy model was applied to investigate the efficacy of prevention undesirable epidural fibrosis. The Animal Care and Use Committee of the School of Medicine, Shanghai Jiao Tong University approved all experimental animal procedures and animal care (No. 20180901). Male Sprague-Dawley rats (12-week-old) were anesthetized with pentobarbital sodium (1%) at 40 mg/kg. Before that, the hair on the back of the rats was removed using a mechanical epilator. After disinfecting the surgical site, a midline approach was made to expose the L2-3 lumbar, and the laminectomy was performed to expose the dura mater with small hemostatic forceps. The surgical area was irrigated with normal saline solution and a sterile gauze was applied to staunch the bleeding. The rats were randomly divided into 3 groups and each group contained 10 rats. Three typical groups were set up in this study: the control group (received without implantation) and two experiment groups (i.e., commercial Interceed films and PVN hydrogels were applied to cover the dura mater). The wounds were stitched layer-by-layer by using 3–0 silk sutures.

Evaluation of epidural fibrosis

After long-term of laminectomy, rats randomly picked in each group were scanned using a 3.0 T magnetic resonance imaging (MRI) system (United Imaging). Basically, MRI included both sagittal and axial T2-weighted imaging sequences, while the epidural fibrosis was evaluated initially based on sagittal T2-weighted images. All rats were then euthanized with an intraperitoneal overdose of pentobarbital sodium. The surgical sites of laminectomy were probed again to further evaluate the degree of epidural fibrosis, which was performed by two orthopedic surgeons according to the Rydell standard.

Histological examination

At a typical post-surgery, the vertebral columns of laminectomy were harvested and fixed in 4% paraformaldehyde solution (pH = 7.4) for 48 h, and subsequently decalcified with 10% EDTA (pH = 7.4) at room temperature for 6 months. After decalcified, the specimens were cut into several pieces along transects and embedded in paraffin. The blocks were sliced into 4 μm sections with a microtome and stained with H&E and MT. A bright-field image of epidural fibrosis was observed and collected using a fluorescence microscope. Here, the vertebral columns with no laminectomy were stained as a positive control.

To analyze fibroblast infiltration in epidural area, the images in each 400 × field were acquired after H&E staining. The fibroblast count for each group was performed using ImageJ software. The collagen content in epidural area was defined by immunofluorescence staining. Briefly, sections were blocked with blocking buffer for 60 min. All sections were incubated with diluted primary antibodies (COL I and III) at 4 °C overnight. Subsequently, the slices were washed with PBS and incubated with corresponding fluorescence secondary antibodies, followed by DAPI treatment to counterstain the nuclei after 90 min. The fluorescence images were obtained with a laser confocal microscope (Nikon A1, Japan), and ImageJ software was applied to measure the collagen content of stained area.

Data availability

The data that support the findings of this study are available from the corresponding authors upon reasonable request. See Author Contributions for the responsible persons for specific data sets.

Author contributions

J.Z. supervised this project. J.Z. and D.Z. captured fleeting allochroic experimental phenomena, conceived the concepts, and designed the whole research; D.Z. and Y.T., synthesized zwitterionic VPES monomers, pVPES with different structural architectures, and all smart devices; D. Z., Y.G., J.G., J.Y., C.M., and J.Z. discussed the allochroic mechanism, conducted theoretical modeling, and molecular dynamics simulations; J.W. lab conducted *in vitro* and *in vivo* experiments for biomedical designs (mice), while L.C. and J.Y. labs completed *in vivo* laminectomy treated with allochroic PVN hydrogels (rats); D.Z. and J.Z. wrote the paper. All authors discussed the results and commented on the manuscript.

Declaration of Competing Interest

The authors declare that they have no known competing financial interests or personal relationships that could have appeared to influence the work reported in this paper.

Acknowledgements

J.Z. thanks financial supports from NSF (1825122 and 1806138) and ACS-PRF (65277-ND7). J.Y. acknowledges the support from National Natural Science Foundation of China (No. 52073255) and Natural Science Foundation of Zhejiang Province (No. LZ20E030004). We really appreciated the technical assistance from Dr. Shuguang Wang (School of Medicine, Tongji University), Prof. Dianwen Song (Shanghai General Hospital, Shanghai Jiao Tong University), Mr. Guanyue Rao (Department of Mechanical Engineering, University of Akron).

Appendix A. Supplementary data

Supplementary data to this article can be found online at https://doi.org/10.1016/j.mattod.2022.09.001.

References

[1] G. Feng, B. Liu, Acc. Chem. Res. 51 (2018) 1404–1414, https://doi.org/10.1021/acs.accounts.8b00060.
[2] B. Yoon et al., Adv. Mater. 23 (2011) 5492–5497, https://doi.org/10.1002/adma.201103471.
[3] W. Zhang et al., Nat. Commun. 10 (2019) 1559, https://doi.org/10.1038/s41467-019-09556-5.
[4] J. Kobashi, H. Yoshida, M. Ozaki, Nat. Photonics 10 (2016) 389–392, https://doi.org/10.1038/nphoton.2016.66.
[5] Y.M. Yang et al., Chem. Rev. 113 (2013) 192–270, https://doi.org/10.1021/cr2004103.
[6] Y. Song et al., ACS Sensors 6 (2021) 220–228, https://doi.org/10.1021/acssensors.0c02148.
[7] C. Chen et al., Nat. Mater. 20 (2021) 175–180, https://doi.org/10.1038/s41563-020-0797-2.
[8] W.J. Zhao, Z.K. He, B.Z. Tang, Nat. Rev. Mater. 5 (2020) 869–885, https://doi.org/10.1038/s41578-020-0223-z.
[9] D. Zhang et al., J. Mater. Chem. A 8 (2020) 20474–20485, https://doi.org/10.1039/d0ta07390c.
[10] L.D. Blackman et al., Chem. Soc. Rev. 48 (2019) 757–770, https://doi.org/10.1039/c8cs00508g.
[11] A.B. Lowe, C.L. McCormick, Chem. Rev. 102 (2002) 4177–4189, https://doi.org/10.1021/cr020371t.
[12] Q. Liu et al., Nat. Commun. 10 (2019) 5262, https://doi.org/10.1038/s41467-019-13238-7.
[13] D. Zhang et al., J. Colloid Interface Sci. 578 (2020) 242–253, https://doi.org/10.1016/j.jcis.2020.05.122.
[14] X. Hou et al., Nature 519 (2015) 70–73, https://doi.org/10.1038/nature14253.
[15] A.J. Keefe, S.Y. Jiang, Nat. Chem. 4 (2012) 60–64, https://doi.org/10.1038/nchem.1213.
[16] H.S. Choi et al., Nat. Biotechnol. 31 (2013) 148–153, https://doi.org/10.1038/nbt.2468.
[17] W. Zhu et al., Adv. Funct. Mater. 31 (2020) 2007026, https://doi.org/10.1002/adfm.202007026.
[18] S. Fu et al., Adv. Sci. 7 (2020) 2001909, https://doi.org/10.1002/advs.202001909.
[19] N. Chandrasekharan, L.A. Kelly, J. Am. Chem. Soc. 123 (2001) 9898–9899, https://doi.org/10.1021/ja016153j.
[20] Y.R. Chang et al., Nat. Nanotechnol. 3 (2008) 284–288, https://doi.org/10.1038/nnano.2008.99.
[21] W.J. Guan et al., Nat. Commun. 7 (2016) 1–7, https://doi.org/10.1038/ncomms11811.
[22] D. Samanta et al., Nat. Commun. 9 (2018) 1–9, https://doi.org/10.1038/s41467-017-02715-6.
[23] R.J. Wojtecki, M.A. Meador, S.J. Rowan, Nat. Mater. 10 (2011) 14–27, https://doi.org/10.1038/Nmat2891.
[24] P.R. Denish et al., Sci. Adv. 7 (2021) eabe7871, https://doi.org/10.1126/sciadv.abe7871.
[25] Z. Wang et al., Adv. Sci. 7 (2020) 1902688, https://doi.org/10.1002/advs.201902688.
[26] Y. Gong et al., Cell Rep. Phys. Sci. (2021) 100663, https://doi.org/10.1016/j.xcrp.2021.100663.
[27] L.R. Shang et al., J. Am. Chem. Soc. 137 (2015) 15533–15539, https://doi.org/10.1021/jacs.5b10612.
[28] S. Zhu et al., Adv. Mate.r 31 (2019) e1900321.
[29] D. Su et al., Chem. 4 (2018) 1128–1138, https://doi.org/10.1016/j.chempr.2018.02.016.
[30] P. Cabanach et al., Adv. Mater. 32 (2020) e2003013.
[31] E. Leontidis, Curr. Opin. Colloid In 7, 81-91, Pii S1359-0294(02)00010-9 10.1016/S1359-0294(02)00010-9 (2002).
[32] S.W. Xiao et al., Curr. Opin. Chem. Eng. 19 (2018) 86–93, https://doi.org/10.1016/j.coche.2017.12.008.
[33] S.W. Xiao et al., Langmuir 34 (2018) 97–105, https://doi.org/10.1021/acs.langmuir.7b03667.
[34] A. Tourrette et al., Colloid Surface A 352 (2009) 126–135, https://doi.org/10.1016/j.colsurfa.2009.10.014.
[35] A.W. Bridges et al., Biomaterials 29 (2008) 4605–4615, https://doi.org/10.1016/j.biomaterials.2008.08.015.
[36] J. Zhu, X.Z. Zhao, C.J. He, RSC Adv. 5 (2015) 53653–53659, https://doi.org/10.1039/c5ra05571g.
[37] R. Jia et al., Nat. Commun. 10 (2019) 795, https://doi.org/10.1038/s41467-019-08675-3.
[38] X. Shang et al., Nat. Commun. 9 (2018) 3933, https://doi.org/10.1038/s41467-018-06147-8.
[39] Y. Zhou et al., Joule 4 (2020) 2458–2474, https://doi.org/10.1016/j.joule.2020.09.001.
[40] X.-H. Li et al., Joule 3 (2019) 290–302, https://doi.org/10.1016/j.joule.2018.10.019.
[41] H. Yuk et al., Nat. Commun. 8 (2017) 1–12, https://doi.org/10.1038/ncomms14230.
[42] Y.S. Kim et al., Nat. Mater. 14 (2015) 1002–1007, https://doi.org/10.1038/nmat4363.
[43] Y.S. Zhao et al., Sci. Rob. 6 (2021) eabd5483, https://doi.org/10.1126/scirobotics.abd5483.
[44] A.K. Mishra, et al. Science Robotics 5, eaaz3918, 10.1126/scirobotics.aaz3918 (2020).
[45] Y. Kim et al., Nature 558 (2018) 274–279, https://doi.org/10.1038/s41586-018-0185-0.
[46] S. Bhosale et al., Science 313 (2006) 84–86, https://doi.org/10.1126/science.1126524.
[47] C.X. Ma et al., Adv. Funct. Mater. 28 (2018) 1704568, https://doi.org/10.1002/adfm.201704568.
[48] Q.L. Zhu et al., Nat. Commun. 11 (2020) 1–11, https://doi.org/10.1038/s41467-020-18801-1.
[49] T. Bai et al., Nat. Med. 25 (2019) 1566–1575, https://doi.org/10.1038/s41591-019-0601-5.
[50] J.J. Green, J.H. Elisseeff, Nature 540 (2016) 386–394, https://doi.org/10.1038/nature21005.
[51] M. Wu et al., Adv. Mater. 32 (2020) 2005222, https://doi.org/10.1002/adma.202005222.
[52] Y.N. Zhu et al., Adv. Funct. Mater. 30 (2020) 1905493, https://doi.org/10.1002/adfm.201905493.
[53] Y. Wang et al., ACS Nano 14 (2020) 8202–8219, https://doi.org/10.1021/acsnano.0c01658.